

Realization of the Hofstadter Hamiltonian with ultracold atoms in optical lattices

M. Aidelsburger^{1,2}, M. Atala^{1,2}, M. Lohse^{1,2}, J. T. Barreiro^{1,2}, B. Paredes³ and I. Bloch^{1,2}

¹ *Fakultät für Physik, Ludwig-Maximilians-Universität,
Schellingstrasse 4, 80799 München, Germany*

² *Max-Planck-Institut für Quantenoptik,
Hans-Kopfermann-Strasse 1, 85748 Garching, Germany*

³ *Instituto de Física Teórica CSIC/UAM
C/Nicolás Cabrera, 13-15 Cantoblanco, 28049 Madrid, Spain*

We demonstrate the experimental implementation of an optical lattice that allows for the generation of large homogeneous and tunable artificial magnetic fields with ultracold atoms. Using laser-assisted tunneling in a tilted optical potential we engineer spatially dependent complex tunneling amplitudes. Thereby atoms hopping in the lattice accumulate a phase shift equivalent to the Aharonov-Bohm phase of charged particles in a magnetic field. We determine the local distribution of fluxes through the observation of cyclotron orbits of the atoms on lattice plaquettes, showing that the system is described by the Hofstadter model. Furthermore, we show that for two atomic spin states with opposite magnetic moments, our system naturally realizes the time-reversal symmetric Hamiltonian underlying the quantum spin Hall effect, i.e. two different spin components experience opposite directions of the magnetic field.

PACS numbers: 03.65.Vf, 03.75.Lm, 67.85.-d, 73.20.-r

Ultracold atoms in optical lattices constitute a unique experimental setting to study condensed matter Hamiltonians in a clean and well controlled environment [1], even in regimes not accessible to typical condensed matter systems [2]. Especially intriguing is their promising potential to realize and probe topological phases of matter, for example, by utilizing the newly developed quantum optical high-resolution detection and manipulation techniques [3, 4]. One compelling possibility in this direction is the quantum simulation of electrons moving in a periodic potential exposed to a large magnetic field, described by the Hofstadter-Harper Hamiltonian [5, 6]. For a filled band of fermions, this model realizes the paradigmatic example of a topological insulator that breaks time-reversal symmetry – the quantum Hall insulator. Moreover, the atomic realization of time-reversal symmetric topological insulators based on the quantum spin Hall effect [7] promises new insights for spintronic applications.

The direct quantum simulation of orbital magnetism in ultracold quantum gases is, however, hindered by the charge neutrality of atoms, which prevents them from experiencing a Lorentz force. Overcoming this limitation through the engineering of synthetic gauge potentials is currently a major topic in cold-atom research. Artificial magnetic fields were first accomplished using the Coriolis force in a rotating atomic gas [8, 9] and later by inducing Berry's phases through the application of Raman lasers [10, 11]. Recently, staggered magnetic fields in optical lattices were achieved using laser induced tunneling in superlattice potentials [12] or through dynamical shaking [13]. In one dimension, tunable gauge fields have been implemented in an effective “Zeeman lattice” [14] and using periodic driving [15]. Furthermore, the free-space spin Hall effect was observed using Raman dressing [16].

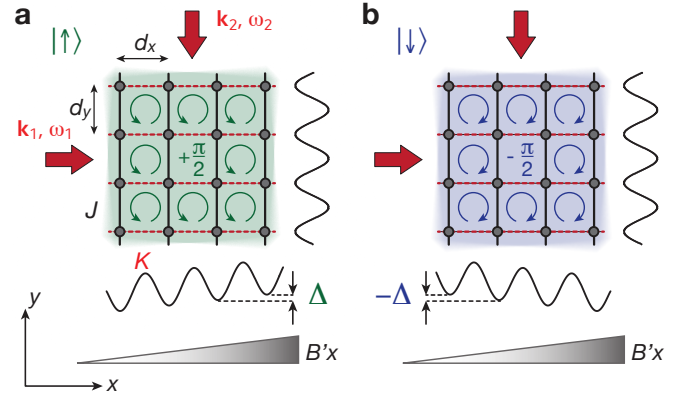


FIG. 1. Experimental setup. The experiment consists of a 3D optical lattice, where the vertical lattice isolates different planes. The lattice constants within each plane are $|\mathbf{d}_i| = \lambda_i/2$, with $i = x, y$. Along y , bare tunneling occurs with strength J , while tunneling along x is inhibited by a magnetic field gradient B' , which introduces an energy offset between neighboring sites of (a) Δ for $|\uparrow\rangle$ atoms and (b) $-\Delta$ for $|\downarrow\rangle$ atoms. An additional pair of laser beams (red arrows) with wave vectors $|\mathbf{k}_1| \simeq |\mathbf{k}_2| = 2\pi/\lambda_K$ and frequency difference $\omega = \omega_1 - \omega_2 = \Delta/\hbar$ is used to restore resonant tunneling with complex amplitude K . This realizes an effective flux of (a) $\Phi = \pi/2$ for $|\uparrow\rangle$ atoms and (b) $-\Phi$ for $|\downarrow\rangle$ atoms.

Despite intense research efforts, 2D optical lattices featuring topological many-body phases have so far been beyond the reach of experiments.

In this Letter, we demonstrate the first experimental realization of an optical lattice that allows for the generation of large tunable homogeneous artificial magnetic fields. The technique is based on our previous work on staggered magnetic fields [12]. The main idea is closely

related to early proposals by Jaksch and Zoller [17] and subsequent work [18, 19]. However, it does not rely on the internal structure of the atom, which makes it applicable to a larger variety of atomic species including fermionic atoms like ^6Li and ^{40}K . We use laser-assisted tunneling in a tilted optical lattice through periodic driving with a pair of far-detuned running-wave beams [20, 21]. In contrast to techniques based on near-resonant laser beams, heating of the atomic cloud due to spontaneous emission is negligible [22]. The position-dependence of the on-site modulation introduced by the running-wave beams leads to a spatially-dependent complex tunneling amplitude. Therefore, an atom hopping around a closed loop acquires a non-trivial phase, which mimics an Aharonov-Bohm phase. In our setup we realize a uniform effective flux of $\Phi = \pi/2$ per plaquette, whose value is fully tunable. We study resonant laser-assisted tunneling in the tilted optical potential and reveal the local distribution of fluxes by partitioning the lattice into isolated four-site square plaquettes. Furthermore, we show that for two spin-states with opposite magnetic moments, $|\uparrow\rangle$ and $|\downarrow\rangle$, our coupling scheme directly gives rise to a non-Abelian $\text{SU}(2)$ gauge field that results in opposite magnetic fields for $|\uparrow\rangle$ and $|\downarrow\rangle$ particles. In the presence of such a gauge field the tight-binding Hamiltonian is time-reversal symmetric and corresponds precisely to the one underlying the quantum spin Hall effect [7, 23].

Our experimental setup consists of an ultracold gas of ^{87}Rb atoms held in a three-dimensional optical lattice created by three mutually orthogonal standing waves of laser light at wavelengths $\lambda_x = \lambda_y = 767\text{ nm}$ and $\lambda_z = 844\text{ nm}$. The depth of the lattice along z is chosen deep enough to suppress tunneling between individual planes, typically $V_z = 30(1) E_{r,z}$, where $E_{r,i} = \hbar^2/(2m\lambda_i^2)$, $i \in \{x, y, z\}$, are the corresponding recoil energies and m is the mass of an atom. A magnetic field gradient B' along x is used to generate a linear potential of amplitude $\pm\Delta$ between neighboring sites, depending on the internal state of the atom [Fig. 1]. We use two Zeeman states with opposite magnetic moments denoted as spin-up $|\uparrow\rangle \equiv |F=1, m_F=-1\rangle$ and spin-down $|\downarrow\rangle \equiv |F=2, m_F=-1\rangle$. For $\Delta \gg J_x$, with J_x being the bare coupling along x , tunneling is inhibited and can be restored resonantly using a pair of far-detuned running-wave beams with a frequency difference $\omega = \Delta/\hbar$ [Fig. 1]. The local optical potential created by these two beams is $V_K(\mathbf{r}) = V_K^0 \cos^2(\mathbf{q}\mathbf{r}/2 + \omega t/2)$, with $\mathbf{q} = \mathbf{k}_1 - \mathbf{k}_2$ being the wavevector difference. This gives rise to a time-dependent on-site modulation term with spatially-dependent phases $\phi_{m,n} = \mathbf{q}\mathbf{R}$, where $\mathbf{R} = m\mathbf{d}_x + n\mathbf{d}_y$ denotes the lattice site (m, n) . In the high-frequency limit, $\hbar\omega \gg J_i$, $i \in \{x, y\}$, the system can be described by an

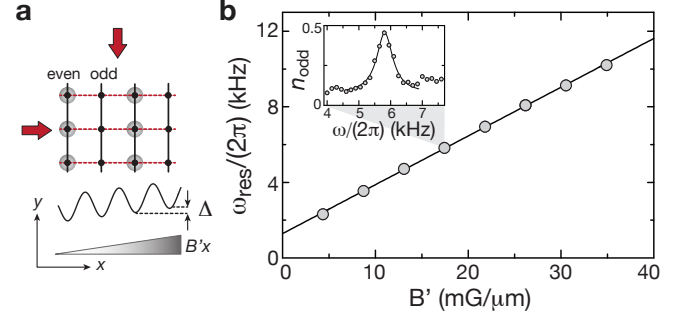


FIG. 2. Laser-assisted tunneling in a tilted optical lattice. (a) Schematic of the initial state used to study laser-assisted tunneling in the presence of a magnetic field gradient B' . Atoms are initially prepared in even sites with at most one atom per lattice site, while odd sites are left empty. (b) Measured frequency difference $\omega_{\text{res}} = \omega_1 - \omega_2$, where atoms resonantly tunnel from even to odd sites, as a function of the magnetic field gradient B' . The finite value at $B' = 0$ is due to a small additional magnetic field gradient [22]. The solid line is a linear fit to our data. The inset shows a typical spectroscopy measurement for $B' = 17.5\text{ mG}/\mu\text{m}$, where the fraction of atoms on odd sites n_{odd} is measured as a function of the frequency difference ω to determine the resonance frequency ω_{res} . The solid line shows the fit of a Lorentzian-function to our data.

effective time-independent Hamiltonian

$$\hat{H}_{\uparrow,\downarrow} = - \sum_{m,n} \left(K e^{\pm i\phi_{m,n}} \hat{a}_{m+1,n}^\dagger \hat{a}_{m,n} + J \hat{a}_{m,n+1}^\dagger \hat{a}_{m,n} \right) + \text{h.c.}, \quad (1)$$

where the sign of the phase factor is positive for $|\uparrow\rangle$ atoms and negative for $|\downarrow\rangle$ atoms. In the limit of $\Delta \gg V_K^0$ the effective coupling strengths along x and y are $K = J_x \mathcal{J}_1(V_K^0/(\sqrt{2}\Delta)) \simeq J_x V_K^0/(2\sqrt{2}\Delta)$ and $J = J_y \mathcal{J}_0(V_K^0/(\sqrt{2}\Delta)) \simeq J_y$, where $\mathcal{J}_\nu(x)$ are the Bessel functions of the first kind [24]. We note that the spin-dependent Peierls phase factors directly arise from the spin-dependent Zeeman coupling to the real applied magnetic field gradient.

For the chosen propagation of the running-wave beams shown in Fig. 1 and $\lambda_K = 2\lambda_y$, we obtain a phase factor $\phi_{m,n} = \pi/2(m+n)$ [22]. Therefore the phase accumulated on a closed path around a plaquette is $\pm\Phi = \pm\pi/2$, depending on the spin of the particle, and the corresponding gauge field is given by $\mathcal{A} = -(\hbar\Phi(x+y)/(d_x d_y), 0, 0) \hat{\sigma}_z$, where $\hat{\sigma}_z$ is the Pauli z -matrix. A different value of the flux Φ could be achieved by changing the wavelength λ_K or the angle between the running-wave beams.

To study laser-assisted tunneling in the presence of the magnetic field gradient B' , we loaded a Bose-Einstein condensate of about 5×10^4 atoms in an initial state, where all atoms populated even sites with at most one atom per site, while odd sites were left empty [Fig. 2(a)]

and [22]. The final lattice depths, $V_x = 5.0(1) E_{rx}$ and $V_y = 40(1) E_{ry}$, were chosen to yield a negligible tunneling along y and a bare tunnel coupling along x of $J_x/h = 0.26(1)$ kHz. Due to the magnetic field gradient, tunneling was inhibited along x and all atoms stayed in even sites. The running-wave beams were then switched on for 4 ms with strength $V_K^0 = 9.9(2) E_{rK}$, where $E_{rK} = \hbar^2/(2m\lambda_K^2)$. Afterwards we measured the fraction of atoms transferred to odd sites n_{odd} as a function of the frequency difference ω for a fixed value of the magnetic field gradient. Even-odd resolved detection was achieved by transferring atoms in odd sites to a higher Bloch band and applying a subsequent band-mapping sequence [22, 25]. As shown in the inset of Fig. 2(b) atoms are transferred resonantly to odd sites when the frequency of the running-wave beams matches the energy offset Δ between neighboring sites. We measured the resonance frequency ω_{res} for various values of the magnetic field gradient and observed a large tunability up to about $\Delta/h \sim 10$ kHz [Fig. 2(b)].

The spatial distribution of the local fluxes induced by the running-wave beams was revealed by a series of measurements in isolated four-site square plaquettes using optical superlattices. This was achieved by superimposing two additional standing waves along x and y with wavelength $\lambda_{li} = 2\lambda_i$, $i \in \{x, y\}$. The resulting potential along x is $V(x) = V_{lx} \sin^2(k_x x/2 + \varphi_x/2) + V_x \sin^2(k_x x)$, where V_{lx} is the depth of the “long” lattice. The superlattice potential along y is given by an analogous expression. The depths of the lattices and the relative phases, φ_x and φ_y , can be controlled independently. For $\varphi_x = \varphi_y = 0$ we realize symmetric double well potentials along x and y to isolate individual plaquettes [Fig. 3]. Due to the presence of the magnetic field gradient, the plaquettes are tilted along x , with an energy offset Δ for $|\uparrow\rangle$ atoms and $-\Delta$ for $|\downarrow\rangle$ atoms. The four sites of the plaquette are denoted as A, B, C, D [Fig. 3]. The experiment started by loading spin-polarized single atoms into the ground state of the tilted plaquettes: $|\Psi_{\uparrow}^0\rangle = (|A\rangle + |D\rangle)/\sqrt{2}$ and $|\Psi_{\downarrow}^0\rangle = (|B\rangle + |C\rangle)/\sqrt{2}$, for $|\uparrow\rangle$ and $|\downarrow\rangle$, respectively [Fig. 3(a) and [22]]. After switching on the running-wave beams the atoms couple to the B and C sites ($|\uparrow\rangle$ atoms) and A and D sites ($|\downarrow\rangle$ atoms). Without the artificial magnetic field, the atoms would oscillate periodically between left and right, but due to the phase imprinted by the running-wave beams the atoms experience a force perpendicular to their velocity similar to the Lorentz force acting on a charged particle in a magnetic field. We measured the time evolution of the atom population on different bonds ($N_{\text{left}} = N_A + N_D$, $N_{\text{right}} = N_B + N_C$, $N_{\text{up}} = N_C + N_D$, and $N_{\text{down}} = N_A + N_B$), with N_q being the atom population per site ($q = A, B, C, D$), by applying the even-odd resolved detection along both directions independently [22]. From this we obtained the mean atom po-

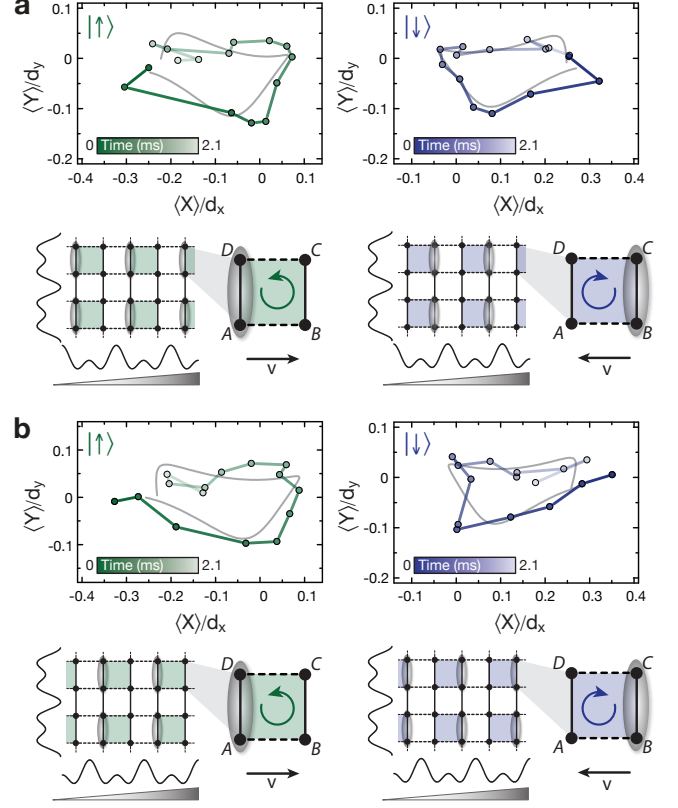


FIG. 3. Quantum cyclotron orbits obtained from the mean atom positions along x and y , $\langle X \rangle / d_x$ and $\langle Y \rangle / d_y$ for $J/K \approx 2$ [22]. Every data point is an average over three individual measurements. The solid gray lines show the fit of the theoretically expected evolution to the data, which was obtained from a numerical calculation solving the time-dependent Schrödinger equation of the 4×4 Hamiltonian. The oscillation amplitudes and offsets were fitted independently along x and y , whereas the time offset $\tau = 0.12(5)$ ms and flux $\Phi = 0.73(5) \times \pi/2$ were fixed (see main text and Supplementary Information [22]). The schematics illustrate the superlattice potentials used to partition the lattice into plaquettes together with the initial state for $|\uparrow\rangle$ atoms (green) and $|\downarrow\rangle$ atoms (blue) and the direction of the flux. The superlattice potential along x is shifted by one lattice constant for the experimental results in (b) with respect to the ones in (a) to demonstrate the uniformity of the artificial magnetic field.

sitions along x and y , $\langle X \rangle = (N_{\text{right}} - N_{\text{left}})d_x/2N$ and $\langle Y \rangle = (N_{\text{up}} - N_{\text{down}})d_y/2N$, with N being the total atom number. As shown in Fig. 3(a), the mean atom position follows a small-scale quantum analog of the classical cyclotron orbit for charged particles. Starting with equally populated sites A and D , spin-up atoms experience a force along y , which is perpendicular to the initial velocity and points towards the lower bond in the plaquette (A and B sites). Spin-down atoms, initially with opposite velocity, also move towards the lower bond. Therefore the chirality of the cyclotron orbit is reversed, re-

vealing the spin-dependent nature of the artificial magnetic field [Fig. 3(a)]. The value of the magnetic flux per plaquette $\Phi = 0.73(5) \times \pi/2$, measured in our previous work [12], is used for the fits in Fig. 3. The difference from $\Phi = \pi/2$, expected for a homogeneous lattice, stems from the smaller distance between lattice sites inside the plaquettes when separated.

To further demonstrate the uniformity of the magnetic field we performed the same set of measurements in plaquettes shifted by one lattice constant along x . This was achieved by changing the relative phase between the two standing waves along x from $\varphi_x = 0$ [Fig. 3(a)] to $\varphi_x = \pi$ [Fig. 3(b)]. The chirality of the obtained cyclotron orbits remained unchanged, which implies that a homogenous magnetic flux is present in the system.

In analogy to the spin Hall effect observed in solid state devices [26], we measured the particle current perpendicular to the initial motion as a function of spin imbalance $n_\uparrow - n_\downarrow$, where n_\uparrow (n_\downarrow) is the fraction of spin-up (-down) atoms. The experimental sequence started from a Mott insulator of unit filling, with each atom prepared in a superposition of $|\uparrow\rangle$ and $|\downarrow\rangle$. We then loaded single atoms into the ground-state of the lower bond of the plaquettes, which has an equal weight on A and B sites [Fig. 4(a)], and measured the mean atom position $\langle X \rangle/d_x$. We obtained an oscillation amplitude for a spin-polarized state of $A_{\langle X \rangle} = -0.28(2)$ for $|\downarrow\rangle$ atoms and $A_{\langle X \rangle} = 0.26(4)$ for $|\uparrow\rangle$ atoms. As can be seen in Fig. 4(b), the evolution is almost perfectly mirrored for the two spin components. The measured oscillation amplitude as a function of the spin imbalance $n_\uparrow - n_\downarrow$ shows that the current depends linearly on the spin imbalance and reverses sign when flipping the spin [Fig. 4(c)].

In conclusion, we have demonstrated a new type of optical lattice that realizes the non-time reversal symmetric Hofstadter-Harper Hamiltonian and the time-reversal symmetric quantum spin Hall Hamiltonian for ultracold atoms in optical lattices. Loading spin-polarized or two-component Fermi gases into this lattice should allow one to directly realize quantum Hall and Z_2 topological insulators with chiral and helical edge states for finite sized systems. This system also opens the path to explore the fractal band structure of the Hofstadter butterfly with ultracold atoms [6]. The lowest band is topologically equivalent to the lowest Landau level and exhibits a Chern number of one [11, 17, 19, 27]. In future experiments the ground-state properties, the effect of the Berry curvature, and topological edge states could be studied [28–30]. The chiral edge modes in this lattice could be directly revealed in ladder systems exposed to a homogeneous magnetic field, which constitute the smallest possible 2D systems in which these states can be observed [31]. Moreover, our work constitutes an important step towards the study of the quantum Hall effect with ultracold atomic gases and the creation of strongly-interacting fractional quantum Hall-like liquids for bosonic and fermionic atoms [32].

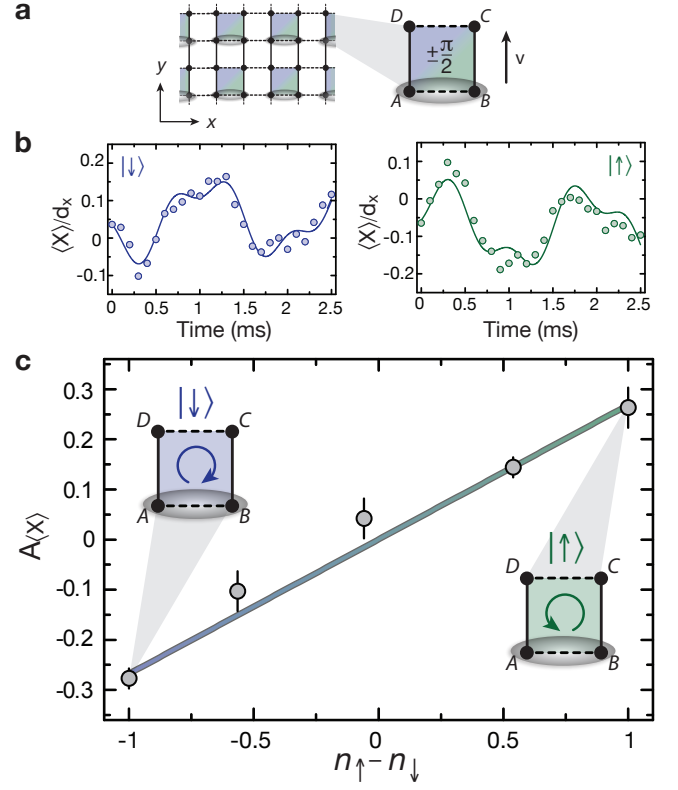


FIG. 4. Particle currents as a function of the spin imbalance of the system. (a) Schematic of the initial state configuration with one atom in a spin-mixture state of $|\downarrow\rangle$ and $|\uparrow\rangle$ in the lower bond of each plaquette [22]. (b) Evolution of the mean atom position along x for all particles in $|\downarrow\rangle$ (blue) and all atoms in $|\uparrow\rangle$ (green) for $J/h = 0.69(1)$ kHz, $K/h = 0.38(1)$ kHz and $\Delta/h = 5.31(5)$ kHz. The solid lines show a fit of the theoretically expected curve to the data obtained using the same method as in Fig. 3 with a time offset $\tau = 0.18(3)$ ms. (c) Oscillation amplitude $A_{\langle X \rangle} = A_{\langle X \rangle}^\downarrow + A_{\langle X \rangle}^\uparrow$ of the mean atom position $\langle X \rangle/d_x$ as a function of the spin imbalance $n_\uparrow - n_\downarrow$. Every data point is an average over two individual measurements. The insets show schematics of the initial states together with the directions of the flux for all atoms in $|\downarrow\rangle$ (blue) and $|\uparrow\rangle$ (green). The solid line is a linear fit to our data, with the offset set to zero. The error bars show the standard deviation of our data.

We thank S. Nascimbène and Y.-A. Chen for their help in setting up the experiment and sharing of their ideas. This work was supported by the DFG (FOR635, FOR801), DARPA (OLE programm) and NIM. M. Aidelsburger was additionally supported by the Deutsche Telekom Stiftung. During the writing of the manuscript, we became aware of similar work carried out in the group of W. Ketterle at MIT [33].

-
- [1] D. Jaksch and P. Zoller, *Ann. Phys.* **315**, 52-79 (2005); I. Bloch, J. Dalibard and W. Zwerger, *Rev. Mod. Phys.* **80**, 885 (2008).
- [2] M. Lewenstein *et al.*, *Adv. Phys.* **56**, 243 (2007); N. Cooper, *Adv. Phys.* **57** (2008); A. Fetter, *Rev. Mod. Phys.* **81**, 647 (2009).
- [3] I. Bloch, J. Dalibard, S. Nascimbène, *Nature Phys.* **8**, 267 (2012)
- [4] W. S. Bakr *et al.*, *Science* **329**, 547 (2010); J. F. Sherson *et al.*, *Nature* **467**, 68 (2010); C. Weitenberg *et al.*, *Nature* **471**, 319 (2011).
- [5] P. Harper, *Proc. Phys. Soc. London, Sect. A* **68**, 874 (1955).
- [6] D. Hofstadter, *Phys. Rev. B* **14**, 2239 (1976).
- [7] B. A. Bernevig and S.-C. Zhang, *Phys. Rev. Lett.* **96**, 106802 (2006).
- [8] K. W. Madison, F. Chevy, W. Wohlleben and J. Dalibard, *Phys. Rev. Lett.* **84**, 806 (2000); J. Abo-Shaeer, C. Raman, J. Vogels and W. Ketterle, *Science* **292**, 476 (2001).
- [9] V. Schweikhard, I. Coddington, P. Engels, V. P. Mogen-dorff, E. A. Cornell, *Phys. Rev. Lett.* **92**, 040404 (2004); V. Bretin, S. Stock, Y. Seurin and J. Dalibard, *ibid* **92**, 050403 (2004).
- [10] Y. Lin *et al.*, *Nature* **462**, 628 (2009).
- [11] J. Dalibard, F. Gerbier, G. Juzeliūnas and P. Öhberg, *Rev. Mod. Phys.* **83**, 1523 (2011). (2010).
- [12] M. Aidelsburger, M. Atala, S. Nascimbène, S. Trotzky, Y.-A. Chen, and I. Bloch, *Phys. Rev. Lett.* **107**, 255301 (2011); M. Aidelsburger, M. Atala, S. Nascimbène, S. Trotzky, Y.-A. Chen, and I. Bloch, *Appl. Phys. B, On-line First* doi:10.1007/s00340-013-5418-1 (2013).
- [13] J. Struck *et al.*, *Science* **333**, 996 (2011).
- [14] K. Jiménez-García *et al.*, *Phys. Rev. Lett.* **108**, 225303 (2012).
- [15] J. Struck *et al.*, *Phys. Rev. Lett.* **108**, 225304 (2012).
- [16] M. C. Beeler *et al.*, *Nature* **498**, 201-204 (2013).
- [17] D. Jaksch and P. Zoller, *New J. Phys.* **5**, 56 (2003).
- [18] F. Gerbier and J. Dalibard, *New J. Phys.* **12**, 033007 (2010).
- [19] E. J. Mueller, *Phys. Rev. A* **70**, 041603 (2004).
- [20] A. Kolovsky, *Europhys. Lett.* **93**, 20003 (2011); C. E. Creffield and F. Sols, *Europhys. Lett.* **101**, 40001 (2013).
- [21] A. Bermudez, T. Schaetz, D. Porras, *Phys. Rev. Lett.* **107**, 150501 (2011).
- [22] Appendix for the estimated heating rate, local phase distribution, experimental sequence, detection methods and numerical simulations.
- [23] N. Goldman, I. Satija, P. Nikolic, A. Bermudez, M. A. Martin-Delgado, M. Lewenstein, and I. B. Spielman, *Phys. Rev. Lett.* **105**, 255302 (2010).
- [24] F. Grossmann and P. Hänggi, *Europhys. Lett.* **18**, 571 (1992); M. Holthaus, *Phys. Rev. Lett.* **69**, 351 (1992).
- [25] J. Sebby-Strabley, M. Anderlini, P. S. Jessen, and J. V. Porto, *Phys. Rev. A* **73**, 033605 (2006); S. Fölling *et al.*, *Nature* **448**, 1029-1032 (2007).
- [26] Y. K. Kato, R. C. Myers, A. C. Gossard, and D. D. Awschalom, *Science* **306**, 1910-1913 (2004); J. Wunderlich, B. Kaestner, J. Sinova, and T. Jungwirth, *Phys. Rev. Lett.* **94**, 047204 (2005).
- [27] N. R. Cooper, *Phys. Rev. Lett.* **106**, 175301 (2011); N. R. Cooper and J. Dalibard, *Europhys. Lett.* **95**, 66004 (2011).
- [28] S. T. Baur and N. R. Cooper, arXiv1306.4611.
- [29] H. M. Price and N. R. Cooper, *Phys. Rev. A* **85**, 033620 (2012).
- [30] N. Goldman, J. Dalibard, A. Dauphin, F. Gerbier, M. Lewenstein, P. Zoller, and I. B. Spielman, *PNAS* **110**(17), 6736-6741 (2013).
- [31] D. Hügel and B. Paredes, arXiv:1306.1190.
- [32] A. S. Sørensen, E. Demler, and M. D. Lukin, *Phys. Rev. Lett.* **94**, 086803 (2005); R. N. Palmer and D. Jaksch, *ibid* **96**, 180407 (2006); M. Hafezi, A. S. Sørensen, E. Demler and M. D. Lukin, *Phys. Rev. A* **76**, 023613 (2007); G. Möller and N. R. Cooper, *Phys. Rev. Lett.* **103**, 105303 (2009).
- [33] H. Miyake, G. A. Siviloglou, C. J. Kennedy, W. C. Burton, and W. Ketterle, arXiv:1308.1431

Appendix

PHOTON SCATTERING RATE

A major advantage of our scheme is the large detuning of the running-wave beams from the atomic transition. For typical experimental parameters we estimated the photon scattering rate to be $2 \times 10^{-3} \text{ s}^{-1}$ corresponding to a lifetime of the sample of several minutes, making the heating due to spontaneous emission negligible.

LOCAL PHASE DISTRIBUTION IN THE LATTICE

As illustrated in Fig. 1 in the main text, bare tunneling with amplitude J occurs along the y direction, while tunneling along the x direction is inhibited by a magnetic-field gradient B' . The pair of far-detuned running-wave beams then restores tunneling along that direction with complex amplitude K . The time-dependent optical potential created by the interference between the two beams gives rise to an on-site modulation with position-dependent phases $\pm\phi_{m,n} = \pm\pi/2(m+n)$, where the phase factors are positive for $|\uparrow\rangle$ atoms and negative for $|\downarrow\rangle$ atoms. The local distribution of phases in the lattice is illustrated in Fig. A1. For atoms in spin states $|\uparrow\rangle$ ($|\downarrow\rangle$), the induced phase increases (decreases) linearly along the vertical and horizontal directions resulting in a total flux of $\Phi = \pi/2$ ($-\Phi$) per plaquette.

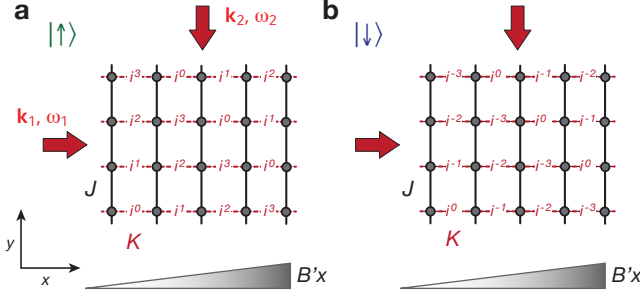


FIG. A1. Schematic drawing of the local phase distribution of the tunneling matrix elements induced by the pair of far-detuned running-wave beams used to restore resonant tunneling along x for (a) $|\uparrow\rangle$ particles and (b) $|\downarrow\rangle$ particles.

EXPERIMENTAL SEQUENCE

Magnetic field gradient

The magnetic field gradient B' used to create the linear potential is produced by a quadrupole magnetic field. Initially the minimum of the quadrupole field is aligned with the position of the atomic cloud. An additional single coil is then used to displace the minimum of the magnetic trap along x from the atom position by generating a magnetic field offset B_0 . However, the magnetic field produced by the coil is not entirely homogeneous but causes a small additional gradient B'_0 . The resulting magnetic field gradient is therefore given by the sum of the two: $B' + B'_0$. For the data depicted in Fig. 2(b) of the main text we vary the strength of the quadrupole field B' without changing the offset field. The finite value of the energy offset between neighboring sites of $\Delta/h = 1.30(4)$ kHz for $B' = 0$ corresponds to B'_0 .

Initial state preparation on even sites

The initial state for the laser assisted-tunneling measurements shown in Fig. 2 of the main text, was prepared such that all atoms populated even sites of the lattice with at most one atom per lattice site. We started by loading a Bose-Einstein condensate in the $|F = 1, m_F = -1\rangle$ -Zeeman state into a 3D optical lattice in the Mott-insulator regime with at most two atoms per lattice site. The lattice was created by the “long lattice” along x ($\lambda_{lx} = 1534$ nm), the “short lattice” along y ($\lambda_y = 767$ nm) and the vertical lattice with wavelength $\lambda_z = 844$ nm. The lattice depths were $V_{lx} = 30(1) E_{rlx}$, $V_y = 20.0(6) E_{ry}$ and $V_z = 20.0(6) E_{rz}$, with $E_{ri} = \hbar^2/(2m\lambda_i^2)$, $i \in \{lx, y, z\}$, being the corresponding recoil energy. Afterwards we applied a filtering sequence where we ramped up the lattices to $V_{lx} = 104(3) E_{rlx}$, $V_y = 100(3) E_{ry}$, $V_z = 120(4) E_{rz}$ and transferred all

atoms to the $|F = 2, m_F = -1\rangle$ state using a rapid adiabatic transfer (Landau-Zener sweep). This was done by applying a microwave field at about 6.8 GHz together with a sweep of the magnetic field offset over the resonance. The sweep was slow enough (10 ms) to stay adiabatic and to achieve almost complete population transfer. In the $|F = 2, m_F = -1\rangle$ state, spin relaxation collisions are strongly enhanced. If two atoms collide at least one of them is transferred to the $F = 1$ manifold and enough energy is released to expel both atoms from the trap [A1, A2]. After 50 ms of waiting time nearly all atoms in doubly occupied sites were removed from the trap and the remaining atoms were transferred back to the $|F = 1, m_F = -1\rangle$ state using a second rapid adiabatic transfer. Then we decreased the lattice depths to $V_{lx} = 52(2) E_{rlx}$, $V_y = 40(1) E_{ry}$ and $V_z = 30(1) E_{rz}$, and ramped up the magnetic field gradient within 200 ms. This time is chosen such that the magnetic field gradient is stable over the duration of the experiment. After that, the short lattice along x was ramped up within 20 ms to $V_x = 40(1) E_{rx}$ in order to load all atoms on the lower energy wells of the tilted double well potentials. After switching off the long lattice within 2 ms we lowered the short lattice to its final value of $V_x = 5.0(1) E_{rx}$. This sequence led to a state where all atoms only populated even sites with at most one atom per lattice site.

Sequence and parameters for the cyclotron orbits

The experimental sequence for the cyclotron measurements shown in Fig. 3 of the main text started by loading a Bose-Einstein condensate in a 3D optical lattice in the Mott-insulator regime created by the two long lattices along x and y and the vertical lattice at depths $V_i = 20.0(6) E_{ri}$, with E_{ri} being the corresponding recoil energy and $i \in \{lx, ly, z\}$. For the filtering sequence described above, we ramped up the lattices to $V_{lx} = 70(2) E_{rlx}$, $V_{ly} = 70(2) E_{rly}$ and $V_z = 120(4) E_{rz}$. After all atoms in doubly occupied sites were lost from the trap we either performed a second Landau-Zener sweep to transfer all atoms to the $|\uparrow\rangle = |F = 1, m_F = -1\rangle$ state (green data points) or we left all remaining atoms in the $|\downarrow\rangle = |F = 2, m_F = -1\rangle$ state (blue data points). Then we lowered the lattice depths to $V_{lx} = 35(1) E_{rlx}$, $V_{ly} = 35(1) E_{rly}$ and $V_z = 30(1) E_{rz}$ and subsequently ramped up the magnetic field gradient to its final value within 250 ms. After ramping up the short lattice along x within 15 ms to $V_x = 40(1) E_{rx}$ all $|\uparrow\rangle$ atoms were loaded in the left wells, while all $|\downarrow\rangle$ atoms were loaded in the right wells. To load the ground-state in the tilted plaquettes we split the long lattice wells along y by switching on the short lattice to $V_y = 10.0(3) E_{ry}$ within 0.1 ms. At the same time we decreased the short lattice along x to its final value $V_x = 7.0(2) E_{rx}$. The dynamics were initiated by

switching on the running-wave beams suddenly. The final trap parameters J, K, Δ were calibrated independently for each measurement. The corresponding values are given in the tables below:

	spin	J/h	K/h	Δ/h
(a)	$ \uparrow\rangle$	0.53(1) kHz	0.27(1) kHz	4.23(3) kHz
	$ \downarrow\rangle$	0.53(1) kHz	0.28(1) kHz	4.56(2) kHz
<hr/>				
	spin	J/h	K/h	Δ/h
(b)	$ \uparrow\rangle$	0.53(1) kHz	0.28(1) kHz	4.91(4) kHz
	$ \downarrow\rangle$	0.53(1) kHz	0.29(1) kHz	4.36(2) kHz

The data points shown in Fig. 3 of the main text are averaged over three individual measurements. The corresponding standard deviations are depicted as error bars in Fig. A2. Residual deviations of the data from the theory curve can most likely be attributed to an imperfect initial state preparation and off-resonant tunneling processes.

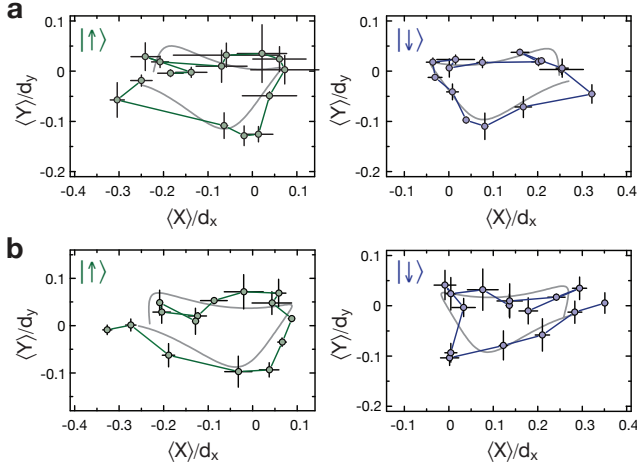


FIG. A2. Cyclotron orbits as shown in Fig. 3(a,b) of the main text. Each data point is averaged over three individual measurements. The error bars depict the corresponding standard deviation.

Spin mixture and initial state preparation

For the measurements shown in Fig. 4 of the main text, we loaded the atoms in a deep 3D optical lattice created by the two long lattices and the vertical lattice, $V_x = 30(1) E_{rlx}$, $V_{ly} = 20.0(6) E_{rly}$ and $V_z = 20.0(6) E_{rz}$. For the filtering sequence they were ramped up to $V_x = 104(3) E_{rlx}$, $V_{ly} = 70(2) E_{rly}$ and $V_z = 120(4) E_{rz}$ and after all doubly occupied sites were lost from the trap, we were left with singly occupied sites and all atoms in the $|\downarrow\rangle$ state. In contrast to the sequence described above,

we stopped the second Landau-Zener sweep at different times to create a superposition of $|\uparrow\rangle$ and $|\downarrow\rangle$. The fraction of atoms in the $|\uparrow\rangle$ and $|\downarrow\rangle$ state was calibrated independently by applying a Stern-Gerlach pulse at the beginning of the time of flight for each sweep configuration. Afterwards we decreased the lattices to $V_{lx} = 52(2) E_{rlx}$, $V_{ly} = 35(2) E_{rly}$ and $V_z = 30(1) E_{rz}$. Similar to the sequence described above we ramped up the short lattice along y within 20 ms at a finite relative phase $\varphi_y \neq 0$ in order to load the atoms in every second site of the superlattice potential along y . Tunneling along that direction was suppressed by the short lattice, $V_y = 40(2) E_{ry}$. The relative phase was then adiabatically changed to $\varphi_y = 0$ within 40 ms, to create a symmetric double well potential. After that we ramped up the magnetic field gradient within 250 ms and subsequently switched on the short lattice along x within 2 ms to its final value $V_x = 6.0(2) E_{rx}$. At this stage of the sequence $|\uparrow\rangle$ atoms were located in A sites, while $|\downarrow\rangle$ atoms were located in B sites. Tunneling along both directions was suppressed either by the magnetic field gradient (x) or a high potential barrier (y). Then the running-wave beams were switched on adiabatically within 7 ms to load the atoms into the ground state of the lower bond of the plaquette, which has an equal weight on A and B sites. Afterwards the dynamics were initiated by lowering the barrier along y within 100 μ s to its final value of $V_y = 9.0(3) E_{ry}$.

SITE-RESOLVED DETECTION

To detect the occupation numbers on the different bonds in the plaquette, we apply two independent band mapping sequences along x and y . In each experimental run only one of the two sequences is applied. For the mapping along x , atoms in sites B and C are transferred to the third Bloch band of the long lattice along x . A subsequent band mapping technique allows us to determine the population in different Bloch bands by counting the corresponding number of atoms [A3, A4]. The colors used in Fig. A3(a) show the connection between the long-lattice Brillouin zones and the corresponding lattice sites for the mapping along x , $N_{\text{left}} = N_A + N_D$ (gray) and $N_{\text{right}} = N_B + N_C$ (blue). To obtain the population in the lower and upper bonds we apply the same technique along y . Figure A3(b) illustrates the connection between the lattice sites and Brillouin zones for the mapping sequence applied along y , with $N_{\text{up}} = N_C + N_D$ (green) and $N_{\text{down}} = N_A + N_B$ (red).

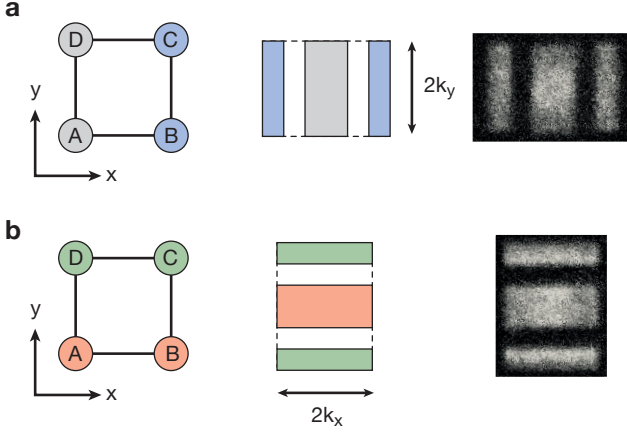


FIG. A3. Schematics of a four-site square plaquette and the corresponding 1-D long-lattice Brillouin zones after applying the mapping sequence (a) along x and (b) along y . The grayscale images show a typical momentum distribution obtained after 10 ms of time-of-flight.

NUMERICAL SIMULATIONS

Fitting functions of the time evolution of the mean atom positions

In order to compare the measured evolutions of the mean atom positions along x and y (shown in Fig. 3 and 4 of the main text) to the theory, we simulate the dynamics of the system by solving the time-dependent Schrödinger equation numerically. The corresponding Hamiltonian is a 4×4 -matrix written in the single-particle basis for each site $\{|A\rangle, |B\rangle, |C\rangle, |D\rangle\}$ with populations respectively given by N_A, N_B, N_C, N_D . The parameters in this Hamiltonian are J, K and Φ . The tunnel couplings J and K between neighboring sites are sketched in Fig. A4 and their values were determined independently via tunneling oscillations (see above). The flux was measured in our earlier work [A5] and determined to be $\Phi = 0.73(5) \times \pi/2$. The obtained time evolutions $X(t)$ and $Y(t)$ are then fitted to our experimental data using the following functions $f_X(t) = X_0 + A_{<X>} \cdot X(t + \tau)$ and $f_Y(t) = Y_0 + A_{<Y>} \cdot Y(t + \tau)$, with $X_0, A_{<X>}, Y_0, A_{<Y>}$ being the fitting variables. A fixed time offset τ is introduced, because the finite ramping times (0.1–0.2 ms) that initiate and freeze the dynamics prevent us from determining the $t = 0$ point a priori. To determine τ , we fitted the evolution for each data set independently and used the average values as fixed time offsets for each figure. For the data shown in Fig. 3 and 4, we obtain average values of 0.12(5) ms and 0.18(3) ms, respectively, which differ slightly because of different experimental sequences.

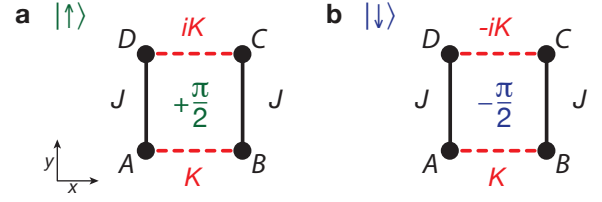


FIG. A4. Schematic drawings of a representative four-site square plaquette showing the tunnel couplings used in the 4×4 Hamiltonian discussed in the text for (a) $|\uparrow\rangle$ particles and (b) $|\downarrow\rangle$ particles.

Monte Carlo sampling of expected cyclotron orbits

Considering the uncertainty in our knowledge of the parameters J, K, Φ , and a potential detuning between lattice sites in each direction of $\Delta_{x,y} = 0(30)$ Hz, we can visualize the agreement between the orbits derived from our model and those from our measurements as follows. First, we assume each parameter J, K, Φ , and $\Delta_{x,y}$ follows a normal distribution with the mean and standard deviation values reported above. Using these distributions, we generate a sample of random parameter values that are then used in our model Hamiltonian to calculate the cyclotron orbits (a sampling procedure sometimes called Monte Carlo sampling). The calculated orbit is then rescaled in amplitude, offset and time delay as described above. By repeating this procedure with 1000 samples, we produce as many cyclotron orbits and plot them together with the data in Fig. A5.

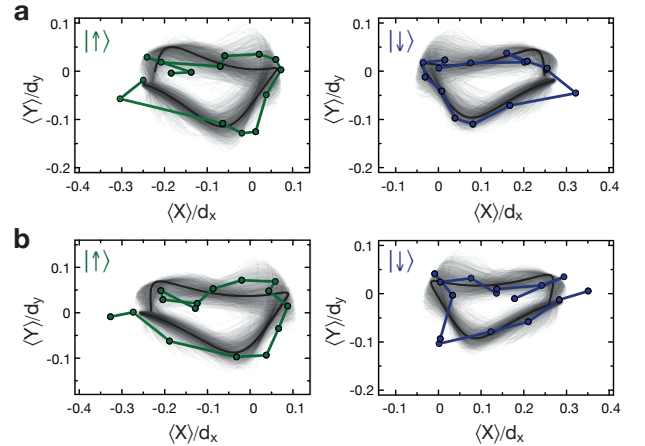


FIG. A5. Cyclotron orbits as shown and described in Fig. 3(a,b) of the main text, with experimentally measured cyclotron orbits (dots connected by green and blue solid lines), expected calculated evolution (black solid lines); but now each including 1000 trajectories from Monte Carlo samples (gray lines) as described in the text.

-
- [A1] C. J. Myatt, E. A. Burt, R. W. Ghrist, E. A. Cornell, and C. E. Wieman, Phys. Rev. Lett. **78**, 586-589 (1997).
- [A2] H. Schmaljohann, M. Erhard, J. Kronjäger, M. Kottke, S. van Staa, L. Cacciapuoti, J. J. Arlt, K. Bongs, and K. Sengstock, Phys. Rev. Lett. **92**, 040402 (2004).
- [A3] S. Fölling *et al.*, Nature **448**, 1029 (2007).
- [A4] J. Sebby-Strabley *et al.*, Phys. Rev. Lett. **98**, 200405 (2007).
- [A5] M. Aidelsburger, M. Atala, S. Nascimbène, S. Trotzky, Y.-A. Chen, and I. Bloch, Phys. Rev. Lett. **107**, 255301 (2011); M. Aidelsburger, M. Atala, S. Nascimbène, S. Trotzky, Y.-A. Chen, and I. Bloch, Appl. Phys. B, Online First **doi:10.1007/s00340-013-5418-1** (2013).